

## Reversible crystalline-to-amorphous phase transformation in monolayer MoS<sub>2</sub> under grazing ion irradiation

Valerius, P.; Kretschmer, S.; V. Senkovskiy, B.; Wu, S.; Hall, J.; Herman, A.; Ehlen, N.; Ghorbani Asl, M.; Grüneis, A.; Krashennnikov, A.; Michely, T.;

Originally published:

January 2020

**2D Materials 7(2020), 025005**

DOI: <https://doi.org/10.1088/2053-1583/ab5df4>

Perma-Link to Publication Repository of HZDR:

<https://www.hzdr.de/publications/Publ-31340>

Release of the secondary publication  
on the basis of the German Copyright Law § 38 Section 4.

# Reversible crystalline-to-amorphous phase transformation in monolayer MoS<sub>2</sub> under grazing ion irradiation

Philipp Valerius,<sup>1,\*</sup> Silvan Kretschmer,<sup>2</sup> Boris V. Senkovskiy,<sup>1</sup> Shilong Wu,<sup>1</sup> Joshua Hall,<sup>1</sup> Alexander Herman,<sup>1</sup> Niels Ehlen,<sup>1</sup> Mahdi Ghorbani-Asl,<sup>2</sup> Alexander Grüneis,<sup>1</sup> Arkady Krasheninnikov,<sup>2,3</sup> and Thomas Michely<sup>1</sup>

<sup>1</sup>*II. Physikalisches Institut, Universität zu Köln, Zùlpicher Straße 77, 50937 Köln, Germany*

<sup>2</sup>*Institute of Ion Beam Physics and Materials Research,*

*Helmholtz-Zentrum Dresden-Rossendorf, 01328 Dresden, Germany*

<sup>3</sup>*Department of Applied Physics, Aalto University, P.O. Box 11100, 00076 Aalto, Finland*

(Dated: October 30, 2019)

By combining scanning tunneling microscopy, low-energy electron diffraction, photoluminescence and Raman spectroscopy experiments with molecular dynamics simulations, a comprehensive picture of the structural and electronic response of a monolayer of MoS<sub>2</sub> to 500 eV Xe<sup>+</sup> irradiation is obtained. The MoS<sub>2</sub> layer is epitaxially grown on graphene/Ir(111) and analyzed before and after irradiation in situ under ultra-high vacuum conditions. Through optimized irradiation conditions using low-energy ions with grazing trajectories, amorphization of the monolayer is induced already at low ion fluences of  $1.5 \times 10^{14}$  ions/cm<sup>2</sup> and without inducing damage underneath the MoS<sub>2</sub> layer. The crystalline-to-amorphous transformation is accompanied by changes in the electronic properties from semiconductor-to-metal and an extinction of photoluminescence. Upon thermal annealing, the re-crystallization occurs with restoration of the semiconducting properties, but residual defects prevent the recovery of photoluminescence.

## I. INTRODUCTION

MoS<sub>2</sub> is a paradigmatic semiconductor in the family of transition metal dichalcogenides (TMDs). Bulk layered MoS<sub>2</sub> and individual sheets have found applications in tribology [1, 2], catalysis [3–5], and as an electronic [6, 7], optoelectronic [8, 9] or spintronic material [10].

Controlled introduction of defects into a [single sheet of MoS<sub>2</sub> \(also: monolayer MoS<sub>2</sub>\)](#) by ion beam irradiation is a powerful tool to alter its morphology [3, 11–22] and the associated changes in the material properties can be beneficial or detrimental, depending on the applications. Examples for beneficial effects are: (i) introduction of S-vacancies created by an Ar plasma dramatically increases the turn-over frequency in the basal plane of MoS<sub>2</sub> for the hydrogen evolution reaction [3]; (ii) low-energy Ar ion irradiation [12] or Ar plasma treatment [13] of MoS<sub>2</sub> prior to metal contact formations gives rise to improved device performance, presumably due to the introduction of defects that short-circuit the metal-MoS<sub>2</sub> Schottky barrier [23] causing thereby a reduction of the contact resistance. Larger fluence particle irradiation induces dramatic changes in the structure and properties of TMDs. Upon 30 keV He<sup>+</sup> irradiation in a helium ion microscope, Fox et al. [14] amorphized few-layer of MoS<sub>2</sub> with doses of  $10^{17} - 10^{18}$  ions/cm<sup>2</sup>, whereby the material became metallic. Using the same tool, similar observations were reported by Stanford et al. [24] for few-layer WSe<sub>2</sub>. Also Zhu et al. [13] observed local phase transformations in MoS<sub>2</sub> under mild Ar plasma treatment from the thermodynamically stable and semiconducting 2H-phase to the metallic 1T-phase. In reverse, Bayer et al. [25] reported

electron beam induced crystallization of thin amorphous MoS<sub>2</sub>.

Ion-irradiation-induced changes in the atomic structure and properties of MoS<sub>2</sub> were noticed already in early studies of the bulk material. Lince et al. [26] showed that, after 1 keV Ne<sup>+</sup> ion irradiation with a fluence of  $4 \times 10^{16}$  ions/cm<sup>2</sup>, the surface of a bulk MoS<sub>2</sub> sample transforms into an amorphous S-depleted state in coexistence with clusters of elemental Mo. Even annealing to 1000 K could not restore a long range order of MoS<sub>2</sub> nor a dissolution of elemental Mo. In contrast, after large fluence 3 keV Ar<sup>+</sup> ion irradiation of bulk MoS<sub>2</sub>, Baker et al. [27] found a homogeneous single amorphous surface with reduced sulfur content.

Here, a new approach is taken to investigate ion irradiation induced changes in monolayer MoS<sub>2</sub>, enabling us to induce a crystalline to amorphous phase transformation at ion fluences of the order of  $1 \times 10^{14}$  ions/cm<sup>2</sup>, 2-3 orders of magnitude lower than in previous experiments. A grazing incidence irradiation geometry is chosen, such that the ion beam has a maximized interaction with the MoS<sub>2</sub> monolayer, but no interaction with the substrate on which the layer is resting on. This implies the absence of undesirable effects like substrate damage, substrate sputtering, ion implantation, and intermixing, which is a precondition for the reversibility of the ion induced transformation of the atomic structure. The MoS<sub>2</sub> monolayer material is synthesized, irradiated and analyzed all in situ under ultra-high vacuum (UHV) without ever exposing the sample to ambient conditions. Thereby, an ultra-clean start material with a marginal point defect density is obtained and well controlled experiments give rise to unambiguous results.

An unexpected finding is that the ion-induced amorphization of monolayer MoS<sub>2</sub> is fully reversible by thermal annealing. The structural phase transformations

---

\* email: valerius@ph2.uni-koeln.de

from the crystalline-to-amorphous-to-crystalline state are accompanied by transitions from semiconducting-to-metallic-to-semiconducting properties.

Scanning tunneling microscopy and -spectroscopy (STM/STS) are chosen as tools to visualize the morphological and electronic changes due to amorphization with a high resolution, low-energy electron diffraction (LEED) as a probe for the crystallinity of the layer, as well as photoluminescence (PL) and Raman spectroscopy to probe sensitively defects and structural changes in the material. Molecular dynamics (MD) simulations are employed to provide atomistic insights into the mechanism of the structural transformations.

## II. METHODS

The STM/STS and LEED experiments were conducted in an UHV chamber with a base pressure below  $1 \times 10^{-10}$  mbar. Ir(111) was cleaned by cycles of 4 keV  $\text{Xe}^+$  exposure at a grazing angle of  $\theta = 75^\circ$  with respect to the surface normal and annealing at 1470 K. Single crystal epitaxial Gr was grown on Ir(111) by room temperature exposure to ethylene till saturation, subsequent thermal decomposition at 1470 K, followed by ethylene exposure through a gas dosing tube at 1220 K for  $\approx 600$  s and with a pressure of  $1 \times 10^{-7}$  mbar measured by a distant ion gauge. Through the gas dosing tube the local sample pressure is enhanced by about a factor of 80 compared to this value.

$\text{MoS}_2$  was grown on Gr/Ir(111) by molecular beam epitaxy (MBE), following the recipe detailed in Ref. 28. Briefly, Mo was deposited at 330 K with a flux of  $F_{\text{Mo}} = 2.6 \times 10^{16} \text{ m}^{-2} \text{ s}^{-1}$  for 500 s, while S was simultaneously sublimated from  $\text{FeS}_2$ . The S flux was controlled through the S pressure set to  $\approx 5 \times 10^{-9}$  mbar. Finally, the sample was annealed at 1050 K in a sulfur pressure of  $2.5 \times 10^{-9}$  mbar for 500 s. The resulting  $\text{MoS}_2$  coverage was  $\approx 0.70$  ML. The coverage is specified in monolayers (ML), where 1 ML corresponds to the full geometrical coverage with a single  $\text{MoS}_2$  layer.

500 eV and 5 keV  $\text{Xe}^+$  ion irradiation were performed at  $\theta = 75^\circ$  and room temperature. The projection of the ion beam onto the surface is within  $\pm 5^\circ$  parallel to a dense-packed [110] direction and aligned with the  $\text{MoS}_2$  zig-zag direction. The ion flux was controlled through a Faraday cup prior to each irradiation experiment. The ion fluence was set to  $1.5 \times 10^{14} \text{ ions cm}^{-2}$  for 500 eV  $\text{Xe}^+$ , i.e. in average 1 out of 7  $\text{MoS}_2$  cells is struck during irradiation by an ion.

STM imaging and STS were conducted at room temperature. STM topographs were obtained with a tunneling voltage  $U_t = -1.5 \text{ V}$  and a tunneling current  $I_t = 50 \text{ pA}$ , if not specified otherwise. They were post-processed using the WSxM software [29]. For spectroscopy, the tip was stabilized at  $I_{\text{stab}} = 2 \text{ nA}$  and  $U_{\text{stab}} = -2.5 \text{ V}$ , while each given spectrum was averaged over 20 single point spectra. Low-energy electron

diffraction (LEED) patterns were digitally recorded over an energy range from about 20 eV to 150 eV.

Analytical potential molecular dynamics (MD) simulations were performed to extract the defect production statistics under  $\text{Xe}$  ion bombardment of  $\text{MoS}_2$  supported by graphene on Ir(111) using the LAMMPS [30] code. The defect production of 500 eV  $\text{Xe}^+$  is assessed by averaging over at least 380 impact points in the irreducible area [31–33] for each angular configuration. A modified Stillinger-Weber potential [34] with a smooth transition to the Ziegler-Biersack-Littmark (ZBL) potential [35] for small distances was used for  $\text{MoS}_2$ . Interactions of carbon atoms in graphene and iridium atoms were accounted for by Tersoff [36] and the embedded-atom method (EAM) [37] potentials, respectively. An attractive interaction between the layers is modeled by a shallow Lennard-Jones potential (Mo-C, C-Ir interaction only), thereby the interlayer distance is maintained. The repulsive part dominating in high-energetic collisions was taken into account by the ZBL potential for all species. The simulated system consisted of about 12,000 atoms, in a simulation box of  $128 \times 74 \times 26 \text{ \AA}^3$  with periodic boundary conditions in the x-y direction. The equations of motion were integrated using an adaptive time step with a maximal size of 0.1 fs and the maximum distance criterion set to 0.001  $\text{\AA}$ . 50,000 time steps were performed for each ion impact simulation.

The sample used for PL and Raman spectroscopy was synthesized in a separate UHV system according to the growth recipe outlined above. After synthesis, it was transferred with a vacuum suitcase to the UHV analysis chamber with a base pressure in the  $10^{-10}$  mbar range [38, 39]. Characterization by LEED, PL, and Raman spectroscopy were conducted prior and after 500 eV  $\text{Xe}^+$  ion irradiation with  $\theta = 75^\circ$ , as well as after annealing of the irradiated sample in S-vapor. PL and Raman spectra were acquired at 10 K using a 532 nm laser. PL spectroscopy was conducted with 6.8 mW laser power to avoid heating, while for Raman spectra we utilized 70 mW for good statistics. The laser was focused with a long-working distance  $\times 50$  objective onto the sample. The energies in Raman and PL spectra were calibrated using the sharp oxygen peak at  $1556 \text{ cm}^{-1}$ , which appears in the spectra due to the part of the laser path outside the vacuum.

## III. RESULTS

### Amorphization and recrystallization

#### *Scanning tunneling microscopy and low-energy electron diffraction*

The key experiment of the present work is visualized in Figs. 1(a)-(c). The STM topograph of Fig. 1(a) displays a coalesced monolayer  $\text{MoS}_2$  on which already small hexagonal-shaped second layer  $\text{MoS}_2$  islands nucleated.

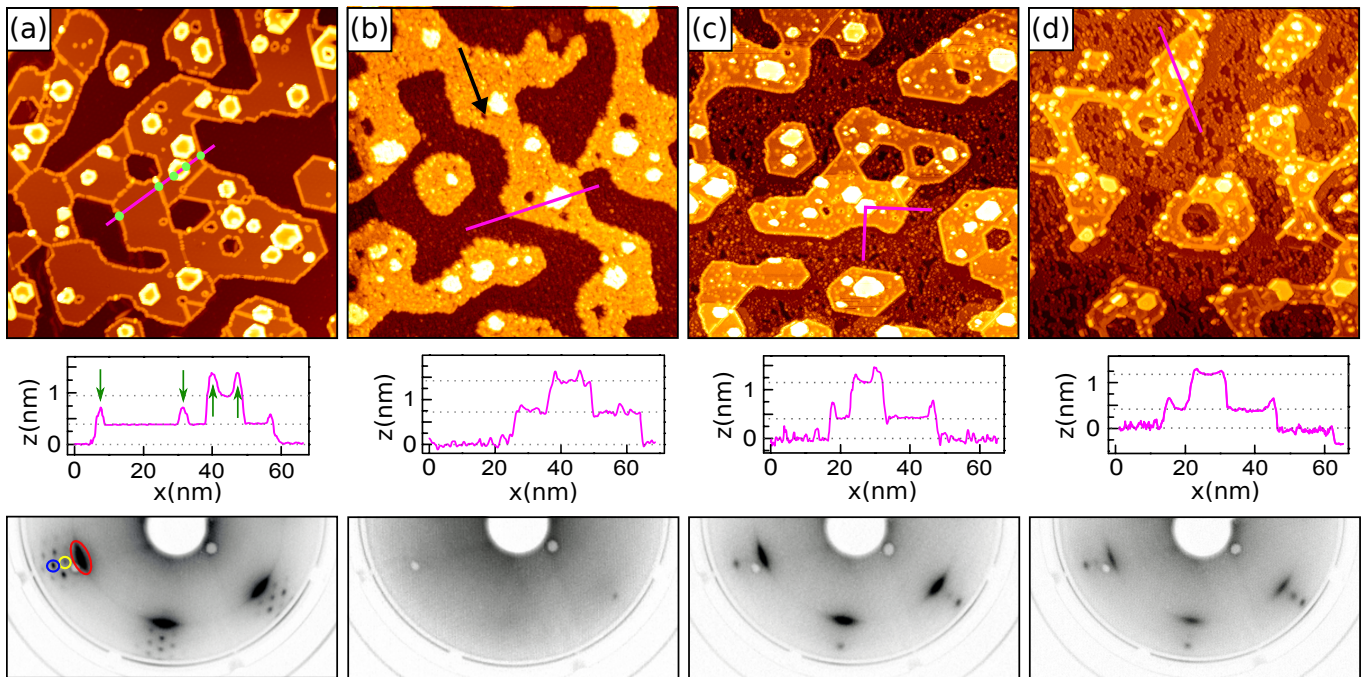


FIG. 1. STM topographs, STM height profiles, and LEED patterns of (a) pristine MoS<sub>2</sub> on Gr/Ir(111); (b) of sample shown in (a) after exposure to a fluence of  $1.5 \times 10^{14}$  ions cm<sup>-2</sup> 500 eV Xe<sup>+</sup> at 300 K; (c) of sample shown in (b) after additional isochronal annealing steps of 300 s at 700 K, 875 K and 1050 K in a sulfur background pressure; (d) of sample shown in (c), after an additional ion fluence of  $1.5 \times 10^{14}$  ions cm<sup>-2</sup> 500 eV Xe<sup>+</sup> and subsequent annealing for 300 s at 1050 K, but in the absence of a sulfur background pressure. Height profiles under topographs are taken along purple lines. Black arrow in (b) indicates projection of the ion beam onto the surface. Image sizes: 164 nm×164 nm; LEED energy: 80 eV.

The edges of the monolayer and bilayer islands are metallic [40] and appear bright in the STM topograph. Additionally, bright lines are visible inside the monolayer, which are also metallic. They are mirror twin and other lower symmetry grain boundaries [41, 42]. Metallic edges and boundaries appear bright in the STM topograph, because tunneling is conducted at  $U_t = -1.5$  V, inside the MoS<sub>2</sub> band gap which ranges from -1.76 eV to +0.77 eV [43] on Gr/Ir(111). Due to the lack of states in the MoS<sub>2</sub> band gap, the tip has to approach closer to the sample to reach the set point current giving rise to a reduced apparent height, while the metallic edge and boundary states provide tunneling electrons, such that their apparent height is close to the geometric thickness of the layer. The height profile taken along the purple line visualizes the situation: the monolayer apparent height is 0.4 nm, while the apparent height of the edges is 0.7 nm, close to the geometric height of 0.61 nm of a monolayer MoS<sub>2</sub>. Note also that the height difference between the monolayer and the bilayer is 0.6 nm in good agreement with the expectations. Finally, tiny vacancy islands and a few point defects are visible through their bright rim or as bright dots. We note that angle resolved photoemission measurements of a similar sample fully confirmed excellent epitaxy and the monolayer nature of our sample [39].

The LEED pattern in Fig. 1(a) corresponding to the sample visualized by the STM topograph displays first order Gr and Ir spots, of which example spots are marked

with blue and yellow circles, respectively. The spots surrounding them are the moiré spots characteristic for single crystal epitaxial Gr/Ir(111) [44]. The intense, elongated spots (example spot encircled red) aligned with Gr and Ir(111) reflections are first order MoS<sub>2</sub> reflections. The full width at half maximum (FWHM) along the circle defined by a constant wave vector  $k$  is  $\pm 7^\circ$ . The spot broadening represents the scatter of the MoS<sub>2</sub> grain orientations with respect to the dense packed Gr and Ir(111) rows.

Subsequently, this sample was irradiated by a fluence of  $1.5 \times 10^{14}$  ions cm<sup>-2</sup> of 500 eV Xe<sup>+</sup> at  $\theta = 75^\circ$  and at 300 K. The STM topograph in Fig. 1(b) depicts the resulting morphology. The projection of the ion beam onto the surface is indicated by an arrow in Fig. 1(b) and within  $\pm 5^\circ$  parallel to a dense-packed [110] direction of Ir(111). The initial morphology consisting of a coalesced monolayer MoS<sub>2</sub> and small hexagonal second layer islands can still be recognized after irradiation. However, the roughness measured on the MoS<sub>2</sub> terraces increased from 0.05 Å for the pristine case (disregarding edges and twin boundaries) to 0.75 Å after irradiation. The surface undulations after irradiation are on the atomic length scale. Enhanced roughness is present not only on monolayer and bilayer MoS<sub>2</sub>, but also on the uncovered Gr layer. The roughness is attributed to atom relocation and sputtering caused by the ion impacts. Remarkably, the bright edge and boundary lines have vanished and the

apparent height of the MoS<sub>2</sub> layer is now uniform with an average around 0.7 nm, i.e. the same height as the initial metallic edge and boundary states displayed [compare height profile along purple line in Fig. 1(a)]. These changes indicate a substantial modification of the electronic structure of the MoS<sub>2</sub> layer towards an increased conductivity at the imaging voltage.

The MoS<sub>2</sub> coverage decreased from 0.71 ML to 0.60 ML through sputtering. Two sputtering mechanisms need to be distinguished: (i) ions impinge on the illuminated step edge, either directly or through reflection at the Gr layer, and may cause violent sputtering through small impact parameters [45]. This mechanism is operative and can be recognized through the rough and rounded appearance of the illuminated MoS<sub>2</sub> edges in Fig. 1(b), while along the shadowed edges still straight portions and characteristic 60° angles can be recognized. (ii) Ions impinge on the terraces of MoS<sub>2</sub> islands and cause sputtering. Whether such events contribute to the loss of coverage is investigated in the next section.

Strikingly, the LEED pattern in Fig. 1(b) displays no more first order MoS<sub>2</sub> or Gr reflections. Only a faint Ir first order reflection encircled yellow is present, indicative of a still crystalline Ir substrate. The lack of MoS<sub>2</sub> and Gr reflections has an evident interpretation: MoS<sub>2</sub> and the uncovered Gr are ion beam amorphized, inhibiting the formation of diffraction spots. Whether the Gr underneath the MoS<sub>2</sub> is damaged or not through the ion beam, cannot be judged on the basis of the LEED pattern. Due to the surface sensitivity of LEED, the strong scattering of Mo (large electron density) and the much weaker of carbon (low electron density) even for an intact Gr lattice underneath a MoS<sub>2</sub> layer no diffraction spots are expected.

After irradiation the sample was successively annealed in S vapor in isochronal steps of 300 s at 700 K, 875 K and 1050 K resulting in the morphology presented in the STM topograph of Fig. 1(c). The MoS<sub>2</sub> has reorganized and displays a similar appearance as after growth. Edge and boundary states reappeared and the height profile along the purple line in Fig. 1(c) displays again the reduced apparent MoS<sub>2</sub> layer height characteristic for the semi-conducting MoS<sub>2</sub>. The MoS<sub>2</sub> islands re-exhibit a smooth surface, though tiny vacancy islands and a substantially larger number of bright point defects are present, when compared to the pristine case as shown by the STM topograph in Fig. 1(a). By annealing, the coverage of MoS<sub>2</sub> decreased only marginally from 0.60 ML for the amorphized layer to 0.58 ML for the crystalline layer. The STM data on the intermediate annealing steps of 700 K and 875 K together with well resolved images of the Gr damage are provided in the Supporting Information as Fig. S1.

In the corresponding LEED pattern of Fig. 1(c), the first order MoS<sub>2</sub> spots reappear in similar intensity and with similar angular spread as for pristine MoS<sub>2</sub> (an example spot is encircled red). The reappearance of the MoS<sub>2</sub> spots makes the recrystallization of the ion beam

amorphized MoS<sub>2</sub> obvious. Also Gr spots reappear (an example spot is encircled blue) while the moiré reflections are missing. For Gr, the annealing temperature is sufficient to regain crystallinity, but not sufficient to develop the level of regularity needed for the development of a moiré, consistent with previous experiments on amorphization and recrystallization of Gr on Ir(111) [46]. The STM topograph of Fig. 1(c) reveals in the areas of uncovered Gr indeed disorder caused by vacancy islands and a large number of bright dots indicative of C atoms still displaced.

When this sample is irradiated again and subsequently annealed with the same succession of isochronal steps in the *absence* of an S vapor, the sample restores again to the crystalline state as visible in Fig. 1(d). However, compared to the annealing in an S vapor [compare Fig. 1(c)] two characteristic differences are present: (i) a large number of clusters of larger height are apparent at the MoS<sub>2</sub> island rims and (ii) through annealing the total MoS<sub>2</sub> coverage decreases substantially from 48 ML to 42 ML, much stronger than in the presence of an S vapor. These two differences may be rationalized by assuming that preferential loss of sulfur due to sputtering and subsequent annealing causes excess Mo to aggregate as small metallic clusters at the island rims, thereby giving rise to the MoS<sub>2</sub> coverage decrease. In contrast, annealing in an S vapor largely replenishes sputtered sulfur and prevents losses during heating.

#### *Molecular dynamics simulations*

To obtain insight into the ion-induced structure transformation of the MoS<sub>2</sub> layer and its surprising ability to restore crystallinity upon annealing, we performed molecular dynamics simulations of 500 eV Xe<sup>+</sup> impacts onto MoS<sub>2</sub> on Gr/Ir(111). Both the polar angle  $\theta$  ( $\theta = 75^\circ$  in experiment) and the azimuthal angle  $\phi$  ( $\phi = 30^\circ \pm 7^\circ$  in experiment) were varied.

Fig. 2(a) displays a snapshot of an event with  $\theta = 75^\circ$  and  $\phi = 27.5^\circ$  just after the impact of the ion. The impact resulted in sputtering of 7 sulfur atoms (the highest yield observed in a single event). All sputtered S atoms stem from the top S layer. Neither Mo atoms nor C atoms from the Gr layer underneath were sputtered. The primary ion was reflected as evident from the ion trajectory schematically indicated by the curved arrow, Fig. 2(a). The side view of Fig. 2(b) makes plain that damage in the underlying Gr layer and in the Ir substrate is absent. Fig. 2(c) is a top view of the damaged area 20 ps after the impact, a sufficient time to dissipate the energy of the impact over the whole system, so that the atomic configuration does not more change, unless thermal annealing is done. Undercoordinated Mo atoms (dark blue) and undercoordinated S atoms (brown) are distributed in a beam-amorphized area with a radius  $R_{\text{defective}} \approx 8 \text{ \AA}$ . In conclusion, a substantial number of top layer S atoms are sputtered away and the MoS<sub>2</sub> layer is amorphized in

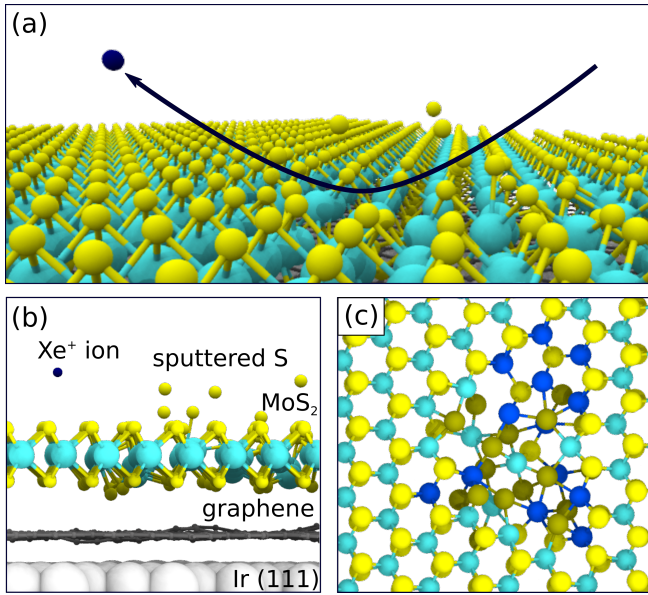


FIG. 2. MD simulation event for a 500 eV  $\text{Xe}^+$  impinging on  $\text{MoS}_2/\text{Gr}/\text{Ir}(111)$  with a polar angle  $\theta = 75^\circ$  and an azimuthal angle of  $\phi = 27.5^\circ$ . (a) Perspective view of the event 3.6 ps after the impact, when sputtering has ceased. The yellow, blue, and dark blue balls represent the sulfur atoms, Mo atoms and the primary ion. The path of the primary ion is highlighted by a curved black arrow. (b) Side view of the same event after highlighting the absence of damage in Gr and the Ir substrate. (c) Top view of the ion beam amorphized area for the same event after 20 ps, when impact energy has dissipated. Undercoordinated Mo atoms are colored dark blue, undercoordinated sulfur atoms are colored brown.

a small area centered at the ion impact. The movie of this and similar events are available in the Supporting Information.

To see how representative the event visualized in Fig. 2 is and how the sputtering evolves with  $\theta$ , Fig. 3(a) displays the sputtering yield  $Y_S$  for S (yellow and red lines) and  $Y_{\text{Mo}}$  for Mo (light and dark blue dashed lines) as a function of the polar angle  $\theta$ . The MD results for  $\phi = 30^\circ$  (yellow, light blue) and the average (red, dark blue) over the three investigated high symmetry directions ( $\phi = 0^\circ, 30^\circ, 60^\circ$ ) are plotted. Apparently,  $Y_S$  has a broad maximum between  $50^\circ$  to  $65^\circ$ , while  $Y_{\text{Mo}}$  has a maximum at somewhat lower angles between  $40^\circ$  to  $60^\circ$ . Quantitatively,  $Y_S$  is larger by at least a factor of 20 compared to  $Y_{\text{Mo}}$ . The vertical dotted line in Fig. 3(a) marks the experimental angle  $\phi = 75^\circ$ . It is apparent that  $Y_{\text{Mo}}$  is zero at  $\theta = 75^\circ$ . In contrast, sulfur sputtering is still substantial at  $\theta = 75^\circ$ . It is  $Y_S = 1.3$  for  $\phi = 30^\circ$ .

With Fig. 3(b) we now take a closer look at the origin of the sputtered sulfur atoms and distinguish sputtered S atoms originating from the top S layer ( $Y_{\text{S,top}}$ , green line, right axis) and sputtered S atoms originating from the bottom S layer ( $Y_{\text{S,bottom}}$ , orange line, right axis) as a function of polar angle  $\theta$ . As expected on the basis of previous MD simulations [31], the overwhelming

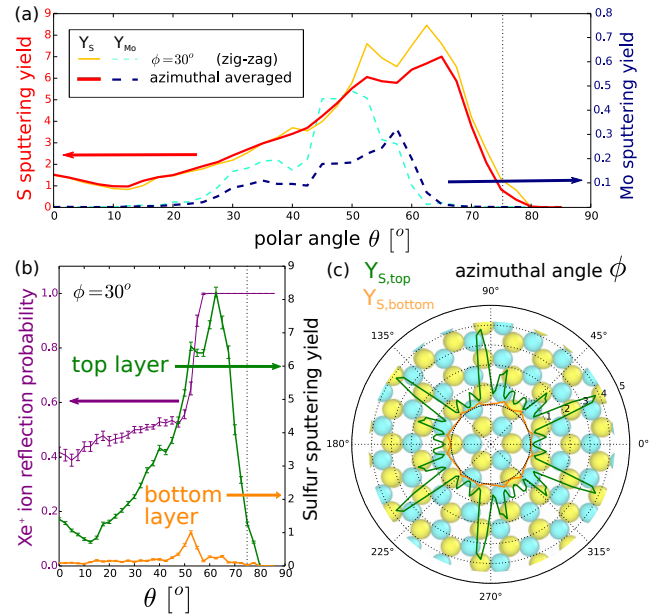


FIG. 3. (a) Dependence of the sputtering yields  $Y_S$  and  $Y_{\text{Mo}}$  on the polar angle  $\theta$  for the azimuthal angle  $\phi = 30^\circ$  (yellow and dashed light blue lines) and the average over  $0^\circ, 30^\circ, 60^\circ$  (red and dashed dark blue lines). (b) Sulfur sputtering yields  $Y_{\text{S,top}}$  (green line, right axis) and  $Y_{\text{S,bottom}}$  (orange line, right axis) for top and bottom layer S atoms, respectively, as a function of polar angle  $\theta$  for  $\phi = 30^\circ$ . Also shown is the ion reflection probability (blue line, left axis) as a function of  $\theta$ . (c) Polar plot of the dependence of  $Y_{\text{S,top}}$  (green line) and  $Y_{\text{S,bottom}}$  (orange line) on  $\phi$  at fixed  $\theta = 75^\circ$  displayed on top of the ball model visualizing the geometry.

majority of all sputtered S atoms stems from the top layer. Only for  $\theta$  around  $50^\circ$  a non-negligible fraction of about 10% originates from the bottom layer. At the experimental angle of  $\theta = 75^\circ$  we find  $Y_{\text{S,bottom}} \approx 0$ , while  $Y_{\text{S,top}} = 1.3$ .

The purple curve in Fig. 3(b) represents the ion reflectivity as a function of polar angle  $\theta$ . At the grazing experimental angle of  $\theta = 75^\circ$  all ions are reflected, consistent with the absence of sputtering for C, Mo, and bottom S. Only at angles below  $60^\circ$  the ion reflectivity drops below 1 and ion penetration of the  $\text{MoS}_2$  takes place. In the small angular range around  $\theta = 50^\circ$ , ion penetration is associated with sputtering of S atoms in the bottom layer.

As the  $\text{MoS}_2$  islands display scatter of  $\pm 7^\circ$  around the dense-packed orientation corresponding to  $\phi = 30^\circ$  our picture is not complete yet, as averaging over the azimuthal angle is necessary to obtain an appropriate estimate of the yields. Fig. 3(c) presents the dependence of  $Y_{\text{S,top}}$  and  $Y_{\text{S,bottom}}$  on  $\phi$  at fixed polar angle of  $\theta = 75^\circ$  (see also Tab. S1 of Supporting information). Apparently, the sputtering yield varies strongly with  $\phi$ . Averaging the yield for an angular range between  $\phi = 22.5^\circ$  and  $\phi = 37.5^\circ$  corresponding to the angular scatter of the  $\text{MoS}_2$  layer yields  $Y_{\text{S,top}} = 2.01$  and

$\bar{Y}_{S,\text{bottom}} = 0.04$  for bottom sulfur. The ratio 50:1 of top to bottom sulfur sputtering indicates almost exclusive sputtering of top layer S. We use the same averaging to obtain an effective ion beam amorphized region with a radius  $R_{\text{defective}} = 6 \text{ \AA}$ , compare with the data presented in Fig. S2 in the Supporting Information.

With the help of the MD simulations, the following picture can be drawn. The primary ion beam removes S atoms from the  $\text{MoS}_2$  top layer and creates an amorphized area with undercoordinated and misplaced Mo and S atoms, whereby the LEED pattern vanishes. Due to the only weak interaction of the ion beam with the Mo atoms as well as the bottom S layer and the absence of sputtering from there, the  $\text{MoS}_2$  layer is not disrupted entirely. The S atoms in the  $\text{MoS}_2$  layer are still coordinated to Mo metal. This is consistent with the presence of an amorphized layer with an apparent STM height close to the geometrical height of the  $\text{MoS}_2$  in Fig. 1(b). Though the Gr layer in between the  $\text{MoS}_2$  islands is subject to sputtering and C atom relocation, our simulations provide evidence that the Gr layer *underneath* the  $\text{MoS}_2$  is not sputtered and remains largely intact. Upon annealing the layer recrystallizes, irrespective of whether S is provided or not. The additional S during annealing heals the S deficiency resulting from the top layer loss during sputtering, while without S supply the excess Mo forms metallic clusters. The recrystallization of the amorphized  $\text{MoS}_2$  on Gr to a high degree of perfection is further evidence for the absence of substantial irradiation damage in the Gr layer underneath. Otherwise strong bonds between Mo and C would have formed, as in irradiated graphene on iridium [47], impeding recrystallization.

According to this picture, ions impinging on the  $\text{MoS}_2$  layer terraces [mechanism (ii) mentioned above] should not cause a shrinkage of the coverage. The only caveat to this conclusion is the fact that when considering the ion dose of  $1.5 \times 10^{14} \text{ ions cm}^{-2}$ , we must assume ions to impinge in the later stages of the exposure time interval onto pre-damaged areas. In contrast, every MD event starts with a perfectly crystalline surface. Therefore, sputtering of bottom S layer and Mo in the experiment cannot be ruled out entirely, and thus this mechanism can still contribute to coverage loss. Nevertheless, the dominant amount of coverage loss is attributed to mechanism (i) mentioned above, namely to sputtering of the illuminated step edges. Considering that the step edge yield may be more than an order of magnitude larger than the terrace yield determined in our MD simulations [45], and taking into account that the flux in a stripe of width 4.6 nm is focused on the illuminated edge, the substantial decrease of coverage becomes understandable. The width of the stripe focusing the flux to the edge is calculated using the geometric model outlined in Ref. 45.

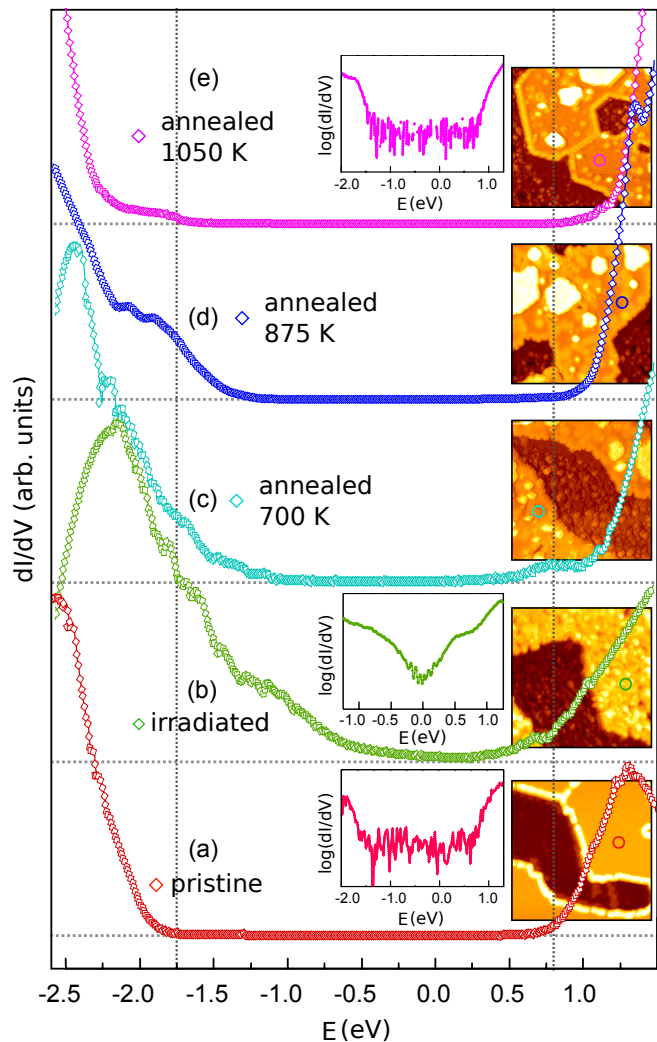


FIG. 4. Evolution of the  $\text{MoS}_2$  constant current  $dI/dV$  tunneling spectra with ion irradiation and annealing. The tip was stabilized at  $I_{\text{stab}} = 2 \text{ nA}$  and  $U_{\text{stab}} = -2.5 \text{ V}$ . Spectra were taken at 300 K. From bottom to top: (a) pristine  $\text{MoS}_2$  on Gr/Ir(111); (b) sample after exposure to a fluence of  $1.5 \times 10^{14} \text{ ions cm}^{-2}$  500 eV  $\text{Xe}^+$ ; (c) sample of (b) annealed for 300 s at 700 K; (d) sample of (c) annealed for 300 s to 875 K; (e) sample of (d) annealed for 300 s to 1050 K. **Left insets** show STM topographs of size  $42 \text{ nm} \times 42 \text{ nm}$ , where locations of point spectra recording are indicated by empty circles. **Middle insets** in (a), (b) and (e) display logarithmic  $dI/dV$  spectra.

### Evolution of electronic and optical properties with amorphization and recrystallization

#### Scanning tunneling spectroscopy

The ion-induced amorphization must be accompanied by changes in the electronic structure of the  $\text{MoS}_2$  layer. We analyze these changes using  $dI/dV$  STS point spectra, of which the intensity corresponds to first approximation to the local density of states (LDOS). For reference,

Fig. 4(a) displays the constant current  $dI/dV$  tunneling spectrum of pristine MoS<sub>2</sub>. The gap between the valence band and the conduction band ranges from -1.8 V to 0.8 V as indicated by vertical dotted lines. The measured gap position and magnitude of 2.6 eV is in-line with our earlier work [43]. Note that the STS measured gap is between the  $\Gamma$ -point valence band maximum and the  $K$ -point conduction band minimum. This gap is larger by about 0.1 eV than the direct band gap between the  $K$ -point extrema (see Ref. 43 for a detailed discussion). For amorphized MoS<sub>2</sub>, the gap largely disappears in the  $dI/dV$  spectrum shown Fig. 4(b). The logarithmic representation of the data  $dI/dV$  data in the inset of Fig. 4(b) in fact suggests metallic behavior, though with a low density of states at the Fermi level. One may therefore conclude that the crystalline, large band gap semiconductor was transformed to an amorphous metal. Also prominent in the  $dI/dV$  spectrum is the increase in the  $dI/dV$ -signal below  $-0.5$  eV, which culminates in a new peak in the LDOS around  $-2.25$  V. The enhanced conductivity at  $U_t = -1.5$  V is consistent with the disappearance of the metallic edge states in the STM topograph of Fig. 1(b) and the increased apparent height of the entire layer through amorphization.

Zhu et al. [13] induced a phase transformation from the 2H to the 1T' phase of MoS<sub>2</sub> through mild Ar plasma treatment with energies well below the displacement threshold for S. Here, we expose MoS<sub>2</sub> to a substantial fluence of ions with energy *large* compared to the displacement threshold, resulting in S sputtering and atom relocation consistent with the absence of any 1T' phase.

Annealing the sample to subsequently higher temperatures reestablishes the band gap gradually, as is apparent from the spectra of Fig. 4(c) after annealing to 700 K and of Fig. 4(d) after annealing to 875 K. The final annealing step to 1050 K gives rise to an  $dI/dV$  point spectrum shown in Fig. 4(e) with a gap of the same size as in the pristine sample [compare Fig. 4(a)]. We note that after the final annealing step still the point spectra show in-gap states when taken close to remaining defects.

It was already noted by Yong et al. [48] and Kodama et al. [49] that S-vacancy formation in MoS<sub>2</sub> is associated with discrete localized in-gap states. Theoretically, Li et al. [3] investigated the effect of ordered S-vacancy structures on band structure and found new vacancy derived bands in the gap, that moved closer to the Fermi level with increasing vacancy concentration, until with 25% vacancies the MoS<sub>2-x</sub> sample becomes metallic. Similar results were also obtained by Iberi et al. [16] for the sister compound MoSe<sub>2</sub>.

As the 500 eV Xe<sup>+</sup> irradiation of MoS<sub>2</sub> at  $\theta = 75^\circ$  applied by us gives rise to S sputtering, the sample certainly develops an S-deficiency which may be rationalized to first approximation as S-vacancies. For an ion fluence of  $1.5 \times 10^{14}$  ions cm<sup>-2</sup> and with  $Y_S \approx 2$  we obtain as an order of magnitude estimate an S-deficiency of 13%, a magnitude where in fact substantial effects are expected.

The closure of the MoS<sub>2</sub> band gap upon ion irradiation is therefore in line with the above mentioned work.

However, preferential sputtering of S and thus S-vacancy creation is not the only effect of ion irradiation. Disorder in lattice, S-bonding and S-concentration are effects not included in the above picture. The disorder will cause a smearing of S-vacancy derived states in energy and in dependence of their precise environment. This explains why we see a continuous extension of the LDOS from the band edges into the gap, rather than an in-gap peak as one might expect for an ordered S-vacancy superstructure.

Even disorder alone, without S-deficiency might give rise to a smearing of the band edges into the gap. After annealing the amorphized layer at 700 K in S-vapor, the stoichiometry of the MoS<sub>2</sub> layer will be very close to nominal. However, as visible in Fig. 4(c) still the LDOS extends into the gap.

In the present experiment, with MoS<sub>2</sub> resting on well conducting Gr, STM measures inherently only the conductivity through, rather than along the two dimensional (2D) material. Although the larger apparent height of the MoS<sub>2</sub> and the LDOS within the band gap after irradiation clearly indicate an enhanced conductivity through the layer at low voltages, disrupted periodicity and disorder will make this material itself unsuitable for lateral transport and diminish its mobility. However, graded ion irradiation underneath contacts with zero irradiation in the channel region or selective amorphization of the top-most layer underneath contacts of a bilayer device might have beneficial effects for the contact resistance, as is made plausible by the work of Cheng et al. [12] or Zhu et al. [13].

#### *Optical properties and Raman spectroscopy*

In order to investigate the effect of the ion irradiation on the optical properties, we conducted ultra-high vacuum photoluminescence (UHV-PL) experiments and compare the spectra of the pristine (light blue), irradiated (violet), and annealed (green) sample in Fig. 5(a). The as-grown MoS<sub>2</sub> on Gr/Ir(111) has a PL peak at 1.95 eV and a narrow FWHM of 13 meV at 10 K, in line with our previous work [39]. Ion-induced amorphization quenches PL in agreement to previous observations on MoS<sub>2</sub> and MoSe<sub>2</sub> monolayers grown on SiO<sub>2</sub>/Si by chemical vapor deposition (CVD) [15, 16], as well as on mechanically exfoliated MoS<sub>2</sub> flakes on SiO<sub>2</sub>/Si [19]. After annealing, PL does not recover in our sample in spite of the fact that PL of CVD-grown MoS<sub>2</sub> on SiO<sub>2</sub>/Si was shown to recover after annealing [15]. We believe that this difference stems from the morphologies and environments of the two MoS<sub>2</sub> samples under consideration. The present MoS<sub>2</sub>/Gr/Ir(111) sample grows epitaxially and has a very narrow PL line-width compared to the PL linewidth of CVD-grown MoS<sub>2</sub> on SiO<sub>2</sub>/Si which has PL FWHM of 53 meV. The narrow PL observed here

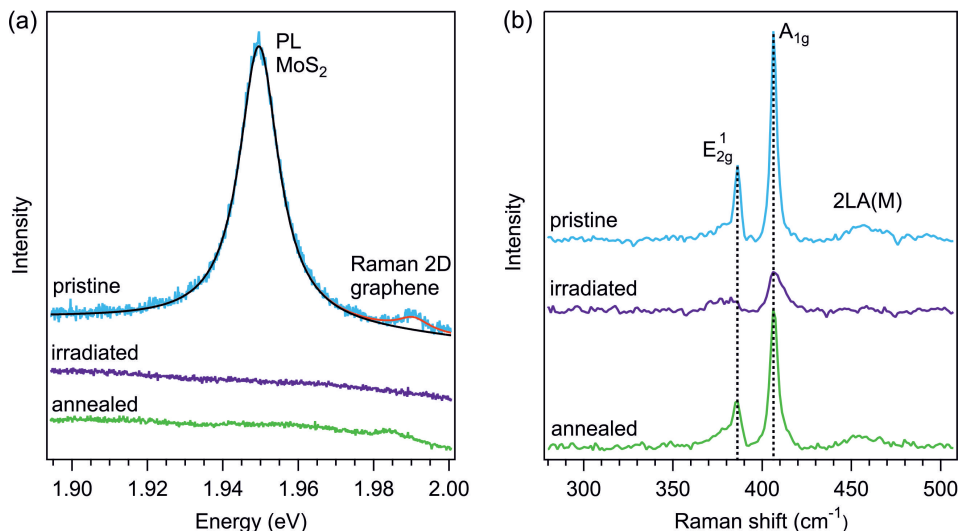


FIG. 5. (a) PL spectra of pristine MoS<sub>2</sub> on Gr/Ir(111) (light blue line), MoS<sub>2</sub> on Gr/Ir(111) irradiated at 300 K with 500 eV Xe<sup>+</sup> at  $\theta = 75^\circ$  (violet line), and the same sample subsequently annealed to 970 K (green line). Black line: fit to the PL peak of the pristine sample by a Lorentzian with a full width at half maximum of 13 meV and center at 1.95 eV. The small peak labeled 'Raman 2D graphene' is the 2D Raman peak of the Gr substrate. (b) Raman spectra of the same sample with identical color code for the preparation conditions. The  $E_{2g}^1$ , the  $A_{1g}$  and the 2LA(M) modes are indicated. Vertical dash lines indicate the positions of the  $E_{2g}^1$  and  $A_{1g}$  modes in the pristine sample.

is an indication of good sample quality. Nevertheless, the intensity (peak area) of the CVD-grown MoS<sub>2</sub> on SiO<sub>2</sub>/Si is  $\sim 6000$  times larger than the PL of MBE-grown MoS<sub>2</sub>/Gr/Ir(111) sample measured under identical conditions. This is a consequence of the metallic substrate and the small island size in MBE-grown sample. The mechanism for PL reduction that relates to the island size is the fact that excitons can diffuse on the island and recombine non-radiatively when reaching the metallic edge of the island. The size of MoS<sub>2</sub> islands of the present MBE-grown sample is smaller compared to the island size of CVD-grown MoS<sub>2</sub>/SiO<sub>2</sub>. Exciton diffusion depends critically on the exciton density [50] and temperature [51]. The relevant PL experiments have been performed on exfoliated TMDC flakes that are freestanding or supported by SiO<sub>2</sub> [50, 51] and therefore a direct quantitative comparison of diffusion lengths in the present system is difficult. Nevertheless, for encapsulated WSe<sub>2</sub> monolayers, diffusion lengths between 360 nm (300 K) and 1.5  $\mu\text{m}$  have been reported [51]. We believe that this process could be particularly important for the present MoS<sub>2</sub>/Gr/Ir(111) samples, because the typical island diameter is at least one order of magnitude smaller than the reported diffusion lengths of the exciton. The metallic edge of an MoS<sub>2</sub> island might therefore provide effective quenching site for the excitons.

The small MoS<sub>2</sub> islands in the present sample are also more sensitive to residual damage after annealing. This is so because the exciton is confined to the island and if the island size is sufficiently small, a single defect does not leave an unperturbed area with a size that allows hosting an exciton. We thus need to compare the average defect separations to the exciton's wavefunction diameter. If

the two numbers are equal to each other, we can expect a change of the PL or even quenching of the PL.

The defect density was estimated by STM and we found that it depends on the annealing temperature. For 875 K annealing temperature we observed one defect within an MoS<sub>2</sub> area of 3.2 nm x 3.2 nm. For a larger annealing temperature of 1050 K we observe one defect in an area of 4.5 nm x 4.5 nm. The annealing temperature was 970 K for the sample whose PL and Raman spectra are shown in Fig. 5. This means that our defect separation will be in between these two values. Let us now compare this separation to the spatial extent of the exciton wavefunction. There are no experimental or theoretical data on the present system but the extent of the exciton wavefunction of a related system (hBN encapsulated WS<sub>2</sub>) has been studied [52]. An exciton of WS<sub>2</sub> in the 1s ground state has a diameter of 4 nm [52]. Thus, the average separation between two defects is in the order of the exciton wavefunction and we speculate that the defect density we have is already sufficient to quench PL. It should be noted that the exciton wavefunction depends strongly on the substrate's dielectric constant and the atomic details of the MoS<sub>2</sub>/Gr/Ir(111) system. Thus, for the precise estimation of the exciton wavefunction of the present system, a detailed calculation that takes into account these issues would be needed.

Let us now look to the effect of sputtering and annealing on the Raman spectra. In Fig. 5(b), we compare the 10 K Raman spectra of the pristine sample (light blue line) with the irradiated (violet line) and annealed (green line) sample. Pristine MoS<sub>2</sub> exhibits two pronounced Raman-active modes – the in-plane  $E_{2g}^1$  mode at

386.3 cm<sup>-1</sup> and the out-of-plane  $A_{1g}$  mode at 406.5 cm<sup>-1</sup> [53], as well as a broad Raman band associated with the double-resonance longitudinal acoustic mode 2LA(M) at 458 cm<sup>-1</sup> [54]. The observed relative Raman shift between the  $E_{2g}^1$  and the  $A_{1g}$  modes of 20.2 cm<sup>-1</sup> is in line with previous results for monolayer MoS<sub>2</sub> on Gr/Ir(111) [39]. Upon irradiation the 2LA(M) mode vanishes, the  $E_{2g}^1$  peak transforms into a broad feature just above the noise level and centered at about 378.5 cm<sup>-1</sup>, and the  $A_{1g}$  drops strongly in intensity becoming broader (with a center at  $\sim 408$  cm<sup>-1</sup>) due to an asymmetry towards higher energy. The intensity drop of all MoS<sub>2</sub> Raman modes indicates structural disorder consistent with amorphization. The observed red-shift of the  $E_{2g}^1$  and the blue-shift of the  $A_{1g}$  phonon frequency was previously reported for MoS<sub>2</sub> in the presence of sulfur vacancies, and it was explained by the modification of the restoring force constant and the total mass of the system [55], as well as by the phonon confinement effect [56, 57]. The characteristic  $E_{2g}^1$  and  $A_{1g}$  phonon modes of MoS<sub>2</sub> recover almost to the initial strength upon annealing [green line in Fig. 5(b)], consistent with amorphization and recrystallization. Noteworthy after annealing there is still an asymmetry of  $E_{2g}^1$  peak toward the lower energies and of the  $A_{1g}$  peak toward the higher energy. This points towards the defects left after the recrystallization.

#### IV. CONCLUSIONS

MD simulations show that at  $\theta = 75^\circ$  grazing incidence of a 500 eV Xe<sup>+</sup> beam on MoS<sub>2</sub> terraces selective sputtering of the top S-layer takes place, while the Mo-layer and the bottom S-layer become disordered, but not sputtered. The supporting Gr layer remains intact and since the Xe<sup>+</sup> projectile is reflected with 100% probability no implantation of Xe atoms takes place.

In consequence, we observe already for ion fluences as low as  $1.5 \times 10^{14}$  ions/cm<sup>2</sup> amorphization of a MoS<sub>2</sub> monolayer on Gr/Ir(111) as evidenced by LEED, but without disruption of the monolayer as an entity: the original island structure is preserved in the amorphous state as visible in the STM topography. In the amorphous state, the semiconducting gap of the monolayer is shown by STS to be largely closed by a continuum of in-gap states due to disorder and sulfur deficit. The PL peak of the pristine layer with a FWHM of only 13 meV is fully quenched in the amorphous state and Raman modes either disappear or are strongly diminished.

Due to the island structure of the MoS<sub>2</sub> layer and the grazing incidence of the impinging ion beam, in addition to terrace sputtering investigated in our MD simulations, illuminated MoS<sub>2</sub> edges are efficiently sputtered. This effect largely accounts for the decrease of MoS<sub>2</sub> island coverage, but does not change the global picture. It would be absent for a complete MoS<sub>2</sub> layer.

As the amorphous phase is homogeneous without disruption, as its sulfur deficit is only moderate, and since

the graphene underneath the MoS<sub>2</sub> remained intact upon amorphization, the MoS<sub>2</sub> recovers to the crystalline state by thermal annealing. After treatment at 1050 K, the residual point defect density is 0.05 defects nm<sup>-2</sup> (corresponding to about 4.5 nm separation), the semiconducting gap is fully re-established, and all phonon modes are in intensity again close to the initial value. However, PL does not recover. We have qualitatively explained the absence of PL in the annealed sample by comparing the defect-defect separation to the spatial extent of the exciton wavefunction. The absence of PL is also not at variance with the observation of a fully restored STS curve that we show in Figure 4. This is so because the STS was measured locally in a defect free region. In the PL measurements a larger region is probed, because of the spatial extent of the exciton. Therefore PL reacts sensitively to defects. Finally, the amorphous state recovers to a crystalline semiconducting state, irrespective of whether the thermal annealing is conducted in an S-vapor or not. In the later case additional metallic clusters are created due to the S-deficit in the amorphous phase, or the loss of sulfur during annealing, or both.

To sum up, we demonstrated that it is possible to selectively change the defect concentration or even amorphize the top layer of a heterostructure assembled from 2D materials, without disturbing or damaging the rest of the stack. In a combination with a thermal treatment and a reactive vapor this opens the possibilities to tune the properties of a single 2D layer in a stack in a wide range. This finding is likely to have relevance for future experiments with stacks of 2D layers or even in device prototyping based on such stacks. The method presented here might also provide a path to synthesize so-called Janus material with a MoSSe stoichiometry that has S (Se) on the upper (lower) plane with respect to Mo as realized by Ma et al. [11] and Lu et al. [58]. Such a material could be synthesized by low energy grazing incidence ion irradiation resulting in sputtering of the upper S layer from a MoS<sub>2</sub> sample and subsequently selenizing it.

#### ACKNOWLEDGMENTS

The authors are grateful for the financial support of the Deutsche Forschungsgemeinschaft (DFG) through projects MI581/22-2 *Low-energy ion irradiation of 2D-materials*, KR 4866/2-1 *Functionalization of ultrathin MoS<sub>2</sub> by defect engineering* and the CRC 1238 (project number 277146847, subprojects A01 and B06). AVK also acknowledges the support from the Academy of Finland under projects No. 286279. We further thank the HZDR computing cluster, CSC Finland and PRACE (HLRS, Stuttgart, Germany) for generous grants of CPU time. BVS and AG acknowledge the ERC-grant no. 648589 'SUPER-2D'.

## V. SUPPORT INFORMATION

The Supporting Information includes the movie related to the ion impact event of Fig. 2(a) and movies of similar events for varying ion beam parameters. Additionally, STM topographs of the entire annealing sequence in larger magnification making details of MoS<sub>2</sub> and Gr damage visible, the tabulated data for the  $\phi$ -dependence of  $f Y_{S,top}$  and  $Y_{S,bottom}$  at  $\theta = 75^\circ$ , and finally the radius of the defectice area  $R_{defective}$  are shown.

- [1] J. Martin, C. Donnet, T. Le Mogne, and T. Epicier, *Phys Rev B* **48**, 10583 (1993).
- [2] B. C. Windom, W. Sawyer, and D. W. Hahn, *Tribol Lett* **42**, 301 (2011).
- [3] H. Li, C. Tsai, A. Koh, L. Cai, A. Contryman, A. Frapane, J. Zhao, H. Han, H. Manoharan, F. Abild-Pedersen, *et al.*, *Nat Mater* **15**, 48 (2016).
- [4] K. Chang, Z. Mei, T. Wang, Q. Kang, S. Ouyang, and J. Ye, *ACS Nano* **8**, 7078 (2014).
- [5] Y. Li, H. Wang, L. Xie, Y. Liang, G. Hong, and H. Dai, *J Am Chem Soc* **133**, 7296 (2011).
- [6] B. Radisavljevic, A. Radenovic, J. Brivio, i. Giacometti, and A. Kis, *Nat Nanotechnol* **6**, 147 (2011).
- [7] Q. H. Wang, K. Kalantar-Zadeh, A. Kis, J. N. Coleman, and M. S. Strano, *Nature Nanotechnol* **7**, 699 (2012).
- [8] Z. Yin, H. Li, H. Li, L. Jiang, Y. Shi, Y. Sun, G. Lu, Q. Zhang, X. Chen, and H. Zhang, *ACS Nano* **6**, 74 (2011).
- [9] D. Lien, M. Amani, S. B. Desai, G. H. Ahn, K. Han, J.-H. He, J. W. Ager, M. C. Wu, and A. Javey, *Nat Commun* **9**, 1229 (2018).
- [10] J. Kim, C. Jin, B. Chen, H. Cai, T. Zhao, P. Lee, S. Kahn, K. Watanabe, T. Taniguchi, S. Tongay, *et al.*, *Sci Adv* **3**, e1700518 (2017).
- [11] Q. Ma, M. Isarraraz, C. S. Wang, E. Preciado, V. Klee, S. Bobek, K. Yamaguchi, E. Li, P. M. Odenthal, A. Nguyen, *et al.*, *ACS Nano* **8**, 4672 (2014).
- [12] Z. Cheng, H. Abuzaid, Y. Yu, F. Zhang, Y. Li, S. G. Noyce, N. X. Williams, Y.-C. Lin, J. L. Doherty, C. Tao, *et al.*, *2D Mater* **6**, 034005 (2019).
- [13] J. Zhu, Z. Wang, H. Yu, N. Li, J. Zhang, J. Meng, M. Liao, J. Zhao, X. Lu, L. Du, *et al.*, *J Am Chem Soc* **139**, 10216 (2017).
- [14] D. S. Fox, Y. Zhou, P. Maguire, A. O'Neill, C. O Coileain, R. Gatensby, A. M. Glushenkov, T. Tao, G. S. Duesberg, I. V. Shvets, *et al.*, *Nano Lett* **15**, 5307 (2015).
- [15] Q. Ma, P. M. Odenthal, J. Mann, D. Le, C. S. Wang, Y. Zhu, T. Chen, D. Sun, K. Yamaguchi, T. Tran, *et al.*, *J Phys Condens Matter* **25**, 252201 (2013).
- [16] V. Iberi, L. Liang, A. V. Ievlev, M. G. Stanford, M.-W. Lin, X. Li, M. Mahjouri-Samani, S. Jesse, B. G. Sumpter, S. V. Kalinin, *et al.*, *Sci Rep* **6**, 30481 (2016).
- [17] K. Haynes, R. Murray, Z. Weinrich, X. Zhao, D. Chiappe, S. Sutar, I. Radu, C. Hatem, S. Perry, and K. Jones, *Appl Phys Lett* **110**, 262102 (2017).
- [18] Y. Chen, S. Huang, X. Ji, K. Adepalli, K. Yin, X. Ling, X. Wang, J. Xue, M. Dresselhaus, J. Kong, *et al.*, *ACS Nano* **12**, 2569 (2018).
- [19] S. Bertolazzi, S. Bonacchi, G. Nan, A. Pershin, D. Beljonne, and P. Samori, *Adv Mater* **29**, 1606760 (2017).
- [20] G.-Y. Zhao, H. Deng, N. Tyree, M. Guy, A. Lisfi, Q. Peng, J.-A. Yan, C. Wang, and Y. Lan, *Appl Sci* **9**, 678 (2019).
- [21] L. Madauß, O. Ochedowski, H. Lebius, B. Ban-d'Etat, C. H. Naylor, A. C. Johnson, J. Kotakoski, and M. Schleberger, *2D Mater* **4**, 15034 (2017).
- [22] R. Kozubek, M. Tripathi, M. Ghorbani-Asl, S. Kretschmer, L. Madauß, E. Pollmann, M. O'Brien, N. McEvoy, U. Ludacka, T. Susi, *et al.*, *J Phys Chem Lett* **10**, 904 (2019).
- [23] S. McDonnell, R. Addou, C. Buie, R. M. Wallace, and C. L. Hinkle, *ACS Nano* **8**, 2880 (2014).
- [24] M. G. Stanford, P. R. Pudasaini, A. Belianinov, N. Cross, J. H. Noh, M. R. Koehler, D. G. Mandrus, G. Duscher, A. J. Rondinone, I. N. Ivanov, *et al.*, *Sci Rep* **6**, 27276 (2016).
- [25] B. C. Bayer, R. Kaindl, M. Reza Ahmadpour Monazam, T. Susi, J. Kotakoski, T. Gupta, D. Eder, W. Waldhauser, and J. C. Meyer, *ACS Nano* **12**, 8758 (2018).
- [26] J. R. Lince, T. B. Stewart, M. M. Hills, P. D. Fleischauer, J. A. Yarmoff, and A. Taleb-Ibrahimi, *Surf Sci* **210**, 387 (1989).
- [27] M. Baker, R. Gilmore, C. Lenardi, and W. Gissler, *Appl Surf Sci* **150**, 255 (1999).
- [28] J. Hall, B. Pielić, C. Murray, W. Jolie, T. Wekking, C. Busse, M. Kralj, and T. Michely, *2D Mater* **5**, 025005 (2018).
- [29] I. Horcas, R. Fernández, J. Gomez-Rodriguez, J. Colchero, J. Gómez-Herrero, and A. Baro, *Rev Sci Instr* **78**, 013705 (2007).
- [30] S. Plimpton, *J Comput Phys* **117**, 1 (1995), arXiv:nag.2347 [10.1002].
- [31] M. Ghorbani-Asl, S. Kretschmer, D. E. Spearot, and A. V. Krasheninnikov, *2D Mater* **4**, 025078 (2017).
- [32] J. Knudsen, P. Feibelman, T. Gerber, E. Grånäs, K. Schulte, P. Stratmann, J. Andersen, and T. Michely, *Phys Rev B* **85**, 035407 (2012).
- [33] S. Kretschmer, M. Maslov, S. Ghaderzadeh, M. Ghorbani-Asl, G. Hlawacek, and A. V. Krasheninnikov, *ACS Appl Mater Interfaces* **10**, 30827 (2018).
- [34] J.-w. Jiang, H. S. Park, and T. Rabczuk, *J Appl Phys* **114**, 64307 (2013).
- [35] J. F. Ziegler, J. P. Biersack, M. D. Ziegler, and J. P. Biersack, *Nucl Instruments Methods Phys Res Sect B*, Vol. 268 (MA: Springer, Boston, 1985) pp. 1818–1823.
- [36] S. Munetoh, T. Motooka, K. Moriguchi, and A. Shintani, *Comput Mater Sci* **39**, 334 (2007).
- [37] S. M. Foiles, M. I. Baskes, and M. S. Daw, *Phys Rev B* **33**, 7983 (1986).
- [38] B. V. Senkovskiy, A. V. Fedorov, D. Haberer, M. Farjam, K. A. Simonov, A. B. Preobrajenski, N. Märtensson, N. Atodiresei, V. Caciuc, S. Blügel, *et al.*, *Adv Electron Mater* **3**, 1600490 (2017).
- [39] N. Ehlen, J. Hall, B. V. Senkovskiy, M. Hell, J. Li, A. Herman, D. Smirnov, A. Fedorov, V. Y. Voroshnin, G. Di Santo, *et al.*, *2D Mater* **6**, 011006 (2018).
- [40] M. Bollinger, J. Lauritsen, K. W. Jacobsen, J. K. Nørskov, S. Helveg, and F. Besenbacher, *Phys Rev Lett* **87**, 196803 (2001).
- [41] H.-P. Komsa and A. V. Krasheninnikov, *Adv Electron Mater* **3**, 1600468 (2017).
- [42] W. Jolie, C. Murray, P. S. Weiß, J. Hall, F. Portner, N. Atodiresei, A. V. Krasheninnikov, C. Busse, H.-P. Komsa, A. Rosch, *et al.*, *Phys Rev X* **9**, 011055 (2019).
- [43] C. Murray, W. Jolie, J. A. Fischer, J. Hall, C. van Efferen, N. Ehlen, A. Grüneis, C. Busse, and T. Michely, *Phys Rev B* **99**, 115434 (2019).
- [44] A. N'Diaye, J. Coraux, T. N. Plasa, C. Busse, T. Michely, *et al.*, *New J Phys* **10**, 043033 (2008).
- [45] H. Hansen, C. Polop, T. Michely, A. Friedrich, and H. M. Urbassek, *Phys Rev Lett* **92**, 246106 (2004).

- [46] C. Herbig, E. Åhlgren, U. Schröder, A. Martínez-Galera, M. Arman, J. Kotakoski, J. Knudsen, A. Krasheninnikov, and T. Michely, *Phys Rev B* **92**, 085429 (2015).
- [47] S. Standop, O. Lehtinen, C. Herbig, G. Lewes-Malandrakis, F. Craes, J. Kotakoski, T. Michely, A. V. Krasheninnikov, and C. Busse, *Nano Lett* **13**, 1948 (2013).
- [48] K. S. Yong, D. M. Otalvaro, I. Duchemin, M. Saeys, and C. Joachim, *Phys Rev B* **77**, 205429 (2008).
- [49] N. Kodama, T. Hasegawa, T. Tsuruoka, C. Joachim, and M. Aono, *Jpn J Appl Phys* **51**, 06FF07 (2012).
- [50] M. Kulig, J. Zipfel, P. Nagler, S. Blanter, C. Schüller, T. Korn, N. Paradiso, M. M. Glazov, and A. Chernikov, *Phys Rev Lett* **120**, 207401 (2018).
- [51] F. Cadiz, C. Robert, E. Courtade, M. Manca, L. Martinelli, T. Taniguchi, K. Watanabe, T. Amand, A. C. H. Rowe, D. Paget, B. Urbaszek, and X. Marie, *Appl Phys Lett* **112**, 152106 (2018).
- [52] J. Zipfel, J. Holler, A. A. Mitioglu, M. V. Ballottin, P. Nagler, A. V. Stier, T. Taniguchi, K. Watanabe, S. A. Crooker, P. C. M. Christianen, T. Korn, and A. Chernikov, *Phys Rev B* **98**, 075438 (2018).
- [53] J. Ribeiro-Soares, R. M. Almeida, E. B. Barros, P. T. Araujo, M. S. Dresselhaus, L. G. Cançado, and A. Jorio, *Phys Rev B* **90**, 115438 (2014).
- [54] B. R. Carvalho, Y. Wang, S. Mignuzzi, D. Roy, M. Terrones, C. Fantini, V. H. Crespi, L. M. Malard, and M. A. Pimenta, *Nat Commun* **8**, 14670 (2017).
- [55] W. M. Parkin, A. Balan, L. Liang, P. M. Das, M. Lamparski, C. H. Naylor, J. A. Rodríguez-Manzo, A. T. C. Johnson, V. Meunier, and M. Drndić, *ACS Nano* **10**, 4134 (2016).
- [56] S. Mignuzzi, A. J. Pollard, N. Bonini, B. Brennan, I. S. Gilmore, M. A. Pimenta, D. Richards, and D. Roy, *Phys Rev B* **91**, 195411 (2015).
- [57] J. Klein, A. Kuc, A. Nolinder, M. Altzschner, J. Wierzbowski, F. Sigger, F. Kreupl, J. J. Finley, U. Wurstbauer, A. W. Holleitner, and M. Kaniber, *2D Mater* **5**, 011007 (2017).
- [58] A.-Y. Lu, H. Zhu, J. Xiao, C.-P. Chuu, Y. Han, M.-H. Chiu, C.-C. Cheng, C.-W. Yang, K.-H. Wei, Y. Yang, *et al.*, *Nature Nanotechnol* **12**, 744 (2017).